3-d linear MHD for acoustic modes and zonal flows

C. Nührenberg[1], K. Hallatschek[2]

Max-Planck-Institut für Plasmaphysik, EURATOM Association,

[1] *Wendelsteinstraße 1, D-17491 Greifswald, Germany*

[2] *Boltzmannstraße 2, D-85748 Garching, Germany*

1 Modeling acoustic modes and zonal flows in the framework of MHD

As in Ref. [1] small electrostatic perturbations about a static MHD equilibrium are studied. In this work the notation of Refs. [2] is used. For electrostatic perturbations $\partial \vec{B}/\partial t = 0$, so that from Faraday's law the perturbed electric field $\vec{E}_1$ is the gradient of a potential Φ_1. Therefore, Ohm's law for the perturbation electric field may be written as $\vec{E}_1 = -\nabla \Phi_1 = \vec{B}_0 \times \partial_t \vec{\xi}$, where $\vec{\xi}$ is the MHD displacement vector. Three scalar perturbation functions related to $\vec{\xi}$ are used: the normal displacement $\xi^s = \vec{\xi} \cdot \nabla s$, and the two components varying in the magnetic surface $s = \text{const}$, $\eta = -F_t' \vec{\xi} \cdot (\nabla\theta - \iota\nabla\phi)$, and $\mu = \sqrt{g} F_t' \vec{\xi} \cdot (\nabla\phi + \iota\nabla\theta)$. Because of $\vec{B}_0 \cdot \nabla\Phi_1 = 0$, the potential of the perturbed electric field is a surface function, i.e. $\Phi_1 = \Phi_1(s)$. Equating the component of $\vec{E}_1$ along $\nabla s \times \vec{B}_0$ shows that $0 = \nabla s \times \vec{B}_0 \cdot \nabla\Phi_1 = (\nabla s \times \vec{B}_0) \cdot (\partial_t \vec{\xi} \times \vec{B}_0) = B_0^2 \partial_t \xi^s$, i.e. $\xi^s \equiv 0$. With this result, taking the component of $\vec{E}_1$ along ∇s shows that $\Phi_{1,s} = -\eta$. Since Φ_1 is a surface function, η must also be a surface function, $\eta = \eta(s)$, with the assumptions made here, i.e. for electrostatic perturbations. With a time dependence $\exp(i\omega t)$, the MHD equation of motion reduces to $-\rho_0\omega^2 \vec{\xi} = -\nabla p_1$, and the pressure equation to $p_1 = -\gamma p_0 \nabla \cdot \vec{\xi}$. Taking the component of the equation of motion along $\vec{B}_0$, a magnetic DE is obtained for $\nabla \cdot \vec{\xi}$, $-\rho_0\omega^2 \sqrt{g} \vec{\xi} \cdot \vec{B}_0 = \gamma p_0 \sqrt{g}\vec{B}_0 \cdot \nabla(\nabla \cdot \vec{\xi})$. Its integrability condition is $\left\langle \sqrt{g} \vec{\xi} \cdot \vec{B}_0 \right\rangle = 0$, where $\langle \bullet \rangle = \int\int \bullet \mathrm{d}\theta \; \mathrm{d}\phi$. With $V' = \langle \sqrt{g} \rangle$ the following relation is obtained from this integrability condition for the perturbation function μ, which appears only in the fluid-compression term, $\langle \mu \rangle = -(IF_p' - JF_t')V' \eta / (IF_t' + JF_p')$.

The CAS3D MHD stability code [2] was used to study these electrostatic perturbations. Two equilibrium cases given in Sec. 2 are investigated with respect to two physical situations: i) the stationary divergence-free flows or zonal flows in Sec. 3 obtained from $\omega = 0$ and ii) finite frequencies of acoustic modes in Sec. 4.

2 Equilibria

The so-called Cyclone DIII-D base case parameter set [3,4] represents local parameters from an ITER-relevant DIIID-D high confinement (H-mode) shot (# 81499 at time $t = 4000$ ms). Similar to Ref. [3], this shot was reconstructed as a circular-cross-section model equilibrium. The ion temperature and electron density profiles given in Fig. 5 of Ref. [4] determine the equilibrium pressure profile $p_0 = 2 n_e T_i$ in Fig. 1 and the equilibrium mass density $\rho_0 = m_\mathrm{p} n_e$ in Fig. 2 ($\rho_0(0) \approx 10^{-7}$ kg/m^3 in a hydrogen plasma). These profiles were used for the configurations studied here. With the pressure profile of Fig. 1 and an axis-value of $p_0(0) = 96132$ N/m^2, an average β of $\langle \beta \rangle = 0.01956$ results (VMEC in its fixed-boundary version [5]). In the reconstruction,
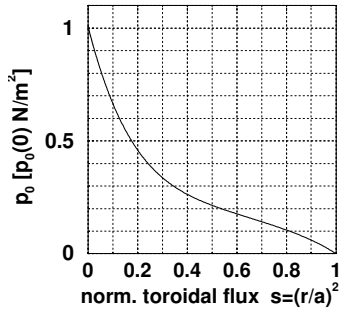
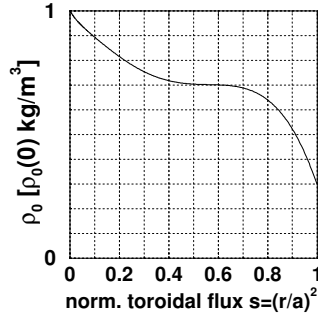*Figure 1: Normalized equilibrium pressure versus normalized toroidal flux.*

Figure 2: Normalized equilibrium mass density versus norm. toroidal flux.
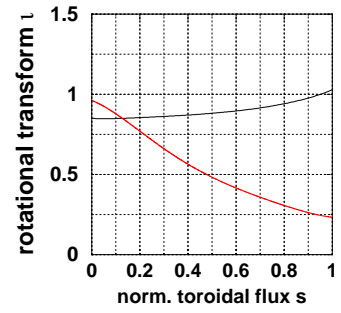

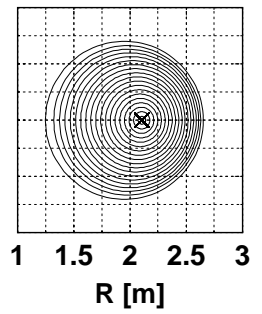*Figure 3: $\iota = 1/q$ in CYCLONE-BASE case (red) and W7-X (black).*

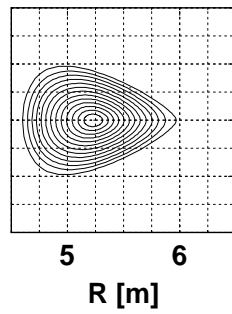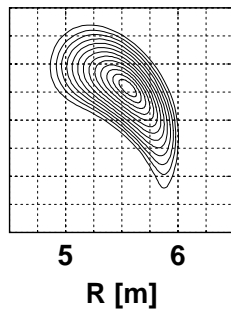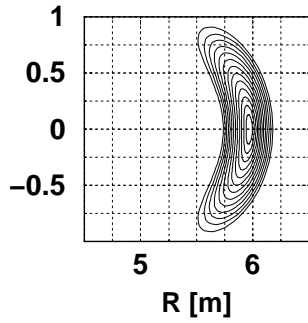*Figure 4: W7-X high-mirror standard case: Flux-surface cross-sections at $\langle\beta\rangle = 0.0205$ as obtained from the 3d MHD-equilibrium code VMEC. Aspect ratio $A \approx 10$, plasma volume $V_{\text{plasma}} \approx 30$ m^3, volume averaged equilibrium magnetic field $\langle B\rangle \approx 1.86$ T.*

Figure 5: CYCLONE-B surfaces at $\langle\beta\rangle = 0.02$. $A \approx 2.8$, $V_{\text{plasma}} \approx 19$ m^3, $\langle B\rangle \approx 2.1$ T.
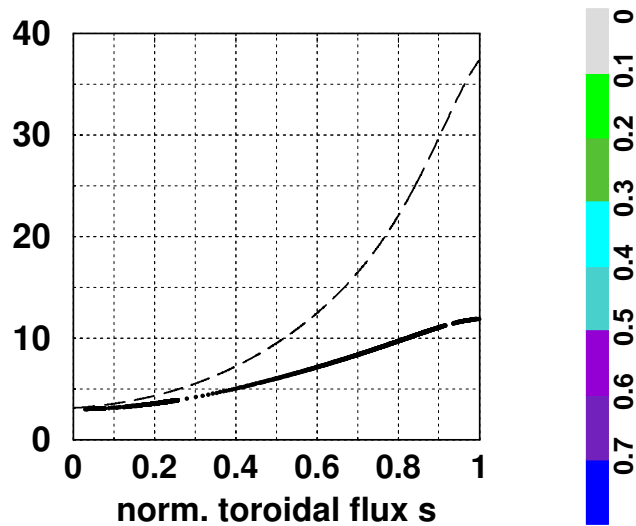

Figure 6: CYCLONE-BASE: For the divergence-free displacements, the ratio of $|\vec{\xi}|^2$ and $|\vec{\xi}_\perp|^2$ (thick-dotted line) equals the Pfirsch-Schlüter term $1+2/\iota^2$ (dashed line) in the vicinity of the magnetic axis. Computation parameters: CAS3D, 1501 radial grid points, harmonics: 1 for η and 7 for μ in the $N = 0$ mode family, $\gamma = 5/3$.
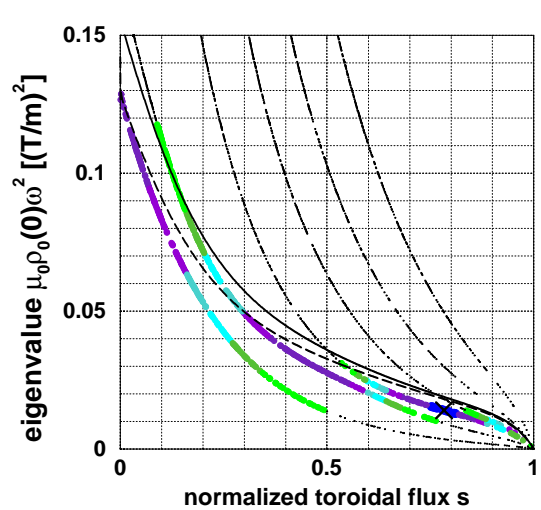
Figure 7: CYCLONE-BASE: Frequencies ω^2 of acoustic modes in units of inverse $\mu_0\rho_0(0)$ versus norm. toroidal flux. Winsor formula (Eq. (1), solid), new estimate (Eq. (2), m=1, n=0, dashed), CAS3D (dotted). Colors for the magnitude of $\xi_\perp$, perturbation with strongest $\xi_\perp$ is at $\times$. Computation parameters: same as in Fig. 6.

$q(0) = 1.04$, $q(a/2) = 1.4$, $q(0.95\,a) = 3.8$, compare Fig. 3. In the reconstructed equilibrium (compare Fig. 5, $R_0 = 1.951$ m, $a = 0.702$ m, $A \approx 2.8$), the plasma current is $I_P = 0.796$ MA, so $\beta_N = (\langle\beta\rangle a^2)/I_P = 1.23$, if $\langle\beta\rangle$ is given in %, and the plasma current in MA.

The W7-X standard high-mirror case is described by the boundary data given in Table IV of Ref. [2] (last entry), here scaled to $R_{00} = 5.5$ m, and $B_0 \approx 2$ T. The flux-surface cross-sections at the beginning, a quarter of, and half of one of the five identical field-periods are shown in Fig. 4, the low-shear rotational transform profile in Fig. 3.

3 Zonal flows

$\omega^2 = 0$ yields incompressible displacements $\vec{\xi}$, i.e. $\nabla \cdot \vec{\xi} = 0$. Thus the structure of these eigenvectors is equivalent to the structure of divergence-free flows and, also, to the current density. For these displacements, evaluation of $|\vec{\xi}|^2/|\vec{\xi}_\perp|^2$ and of the Pfirsch-Schlüter factor $1 + 2/\iota^2$ is compared in Figs. 6 (CYCLONE-BASE), and 9 (W7-X). The results show the correspondence to the Pfirsch-Schlüter factor in the CYCLONE case and the reduction of the parallel flow equivalent to the reduction of the parallel current density in the W7-X case.

Figure 8: $\xi_{||}$ *Fourier amplitudes of acoustic modes; top frame: CYCLONE-BASE,* $\mu_0\rho_0(0)\omega^2 = 0.014$, $W_{kin}(\xi_\perp)/W_{kin} = 0.713$ *(marked* $\times$ *in Fig. 7); bottom frame: W7-X variant,* $\mu_0\rho_0(0)\omega^2 = 0.001$, $W_{kin}(\xi_\perp)/W_{kin} = 0.12$ *(marked* $\times$ *in Fig. 10). Colors:* $n = 0$ *black,* $n = -5$ *red,* $n = -10$ *green,* $n = 5$ *blue,* $n = -15$ *orange.*

4 Acoustic-mode frequencies

In Ref. [1] a large-aspect-ratio tokamak result for the frequency of the lowest node-number axisymmetric acoustic oscillation is given, Eq. (1). The generalization of this formula to a large-aspect-ratio general geometry, in magnetic coordinates, characterized by its differential volume $\sqrt{g}$ and the geometry of its flux surfaces in terms of $|\nabla s|^2$ is found to be Eq. (2). The spectrum of the acoustic-mode frequencies vs. flux surface label as obtained with CAS3D is shown in Figs. 7 and 10. Some low-node oscillations are highlighted together with their corresponding estimates in general geometry, Eq. (2). The Winsor estimate is also indicated.

Nearly quantitative coincidence between the Winsor and the new estimates is observed in the CYCLONE case, they, however, quantitatively fail at low aspect ratio, see Fig. 7. The perturbations

$$\omega_{Winsor}^2 = \frac{2\gamma p_0}{\rho_0 R_0^2}(1 + 0.5\iota^2) \tag{1}$$

$$\omega_{new}^{2\,mn} = \frac{2\gamma p_0}{\rho_0}\frac{\pi^2}{\sqrt{g_{00}^2}}\left[m^2\frac{\sqrt{g_{mn}^2}B_{00}^2}{F_t'^2|\nabla s|_{00}^2} + 2(m\iota + n)^2\frac{F_t'^2}{B_{00}^2}\right] \tag{2}$$

computed with CAS3D may be classified Geodesic Acoustic Mode (GAM), if $\xi_\perp > \xi_{||}$, and sound mode in the case where the flow along $\vec{B}$ dominates. In Fig. 7, the GAM
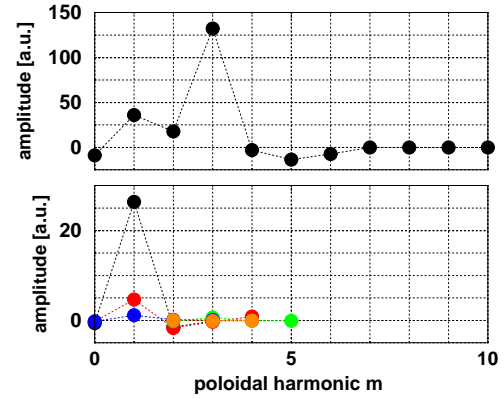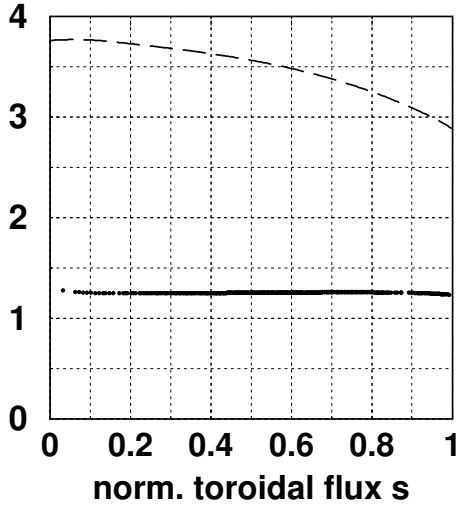
Figure 9: W7-X: For the divergence-free displacements, the ratio of $|\vec{\xi}|^2$ and $|\vec{\xi}_\perp|^2$ (thick-dotted line) is approximately constant and everywhere well below the Pfirsch-Schlüter term $1 + 2/\iota^2$ (dashed line). Computation parameters: CAS3D, 201 radial grid points, harmonics: 1 for η and 56 for μ in the $N = 0$ mode family, $\gamma = 5/3$.
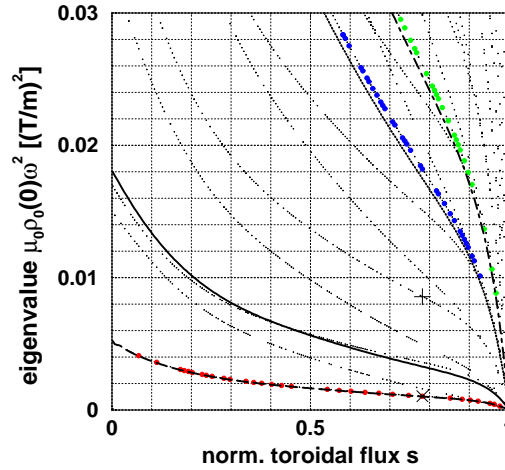
Figure 10: W7-X: Frequencies ω^2 in units of inverse $\mu_0\rho_0(0)$ of acoustic modes versus normalized toroidal flux. Winsor (solid), new [dashed for (1,0); dot-dashed for (0,-5), dotted for (1,-5)], CAS3D [red for (1,0), green for (0,-5), blue for (1,-5) and black dotted for all]. Perturbation with $W_{\mathrm{kin}}(\xi_\perp)/W_{\mathrm{kin}} = 0.12$ (marked $\times$); perturbation with $W_{\mathrm{kin}}(\xi_\perp)/W_{\mathrm{kin}} \approx 0$ (marked $+$). Computation parameters: same as in Fig. 9.

with strongest $\xi_\perp$ is located at $s = 0.78$, it has a frequency of 53 kHz and is essentially $m = 3$, see top frame of Fig. 8, compare [7]. Note that in Ref. [7] the dimensionless factor $\sqrt{2\gamma(1 + T_e/T_i)}$ is absent in the estimate of the GAM frequency, the correct form is given in Eq. (3) of Ref. [6]. In keeping with the results obtained for the stationary flows, the W7-X case indicates strongly reduced frequencies for the $(m,n)=(1,0)$ mode as compared to the Winsor model, see Fig. 10. Further modes (mirror-type, helical-type) are also indicated and are nearly quantitatively described by the generalized large-aspect ratio formula. The largest $\xi_\perp$-values are found for the essentially $m = 1$ perturbations, see Fig. 8 for the mode at 14 kHz, but with $\xi_{||} > \xi_\perp$, these modes are sound polarized rather than of the GAM-type. In summary, a reduction is seen of (i) the acoustic-mode frequency as compared to the Winsor estimate and (ii) the $|\vec{\xi}|^2/|\vec{\xi}_\perp|^2$ term for stationary flows as compared to the Pfirsch-Schlüter factor. The mechanism is different in the two cases studied here. The Shafranov-shift may be responsible for the reduction in the Cyclone B case (low aspect ratio, circular cross-section, significant Shafranov-shift). The geometry may be responsible in the W7-X case (high aspect ratio, reduced Shafranov-shift, 3-d geometry).

•[1] N. Winsor, J.L. Johnson, and J.M. Dawson, Phys. Fluids **11** (11), 2248 (1968). •[2] C. Schwab, Phys. Fluids B **5** (9), 3195 (1993). C. Nührenberg, Phys. Plasmas **3** (6), 2401 (1996). C. Nührenberg, Phys. Plasmas **6** (1), 137 (1999). •[3] A.M. Dimits, *et al.*, Phys. Plasmas **7** (3), 969 (2000). •[4] C.M. Greenfield, *et al.*, Nucl. Fusion **37** (9), 1215 (1997). •[5] S.P. Hirshman, W.I. van Rij, and P. Merkel, Comput. Phys. Commun. **43** , 143 (1986). •[6] K. Hallatschek, and D. Biskamp, Phys. Rev. Lett. **86** (7), 1223 (2001). •[7] M. Jakubowski, *et al.*, Phys. Rev. Lett. **89** (26), 265003 (2002). •